Energy & Environmental Science

Effects of Bubbles on the Electrochemical Behavior of Hydrogen-Evolving Si Microwire Arrays Oriented Against Gravity

Journal:	*Energy & Environmental Science*
Manuscript ID	EE-ART-02-2020-000356.R2
Article Type:	Paper
Date Submitted by the Author:	07-Apr-2020
Complete List of Authors:	Kempler, Paul; California Institute of Technology, Division of Chemistry and Chemical Engineering Coridan, Robert; University of Arkansas Fayetteville, Chemistry and Biochemistry Lewis, Nathan; California Institute of Technology, Chemistry and Chemical Engineering

Effects of Bubbles on the Electrochemical Behavior of Hydrogen-Evolving Si Microwire Arrays Oriented Against Gravity

Paul A. Kempler[1], Robert H. Coridan[2], Nathan S. Lewis[1,3*]

[1]Division of Chemistry and Chemical Engineering, 127-72, 210 Noyes Laboratory, California Institute of Technology, Pasadena, CA 91125

[2]Department of Chemistry and Biochemistry, University of Arkansas, Fayetteville, Arkansas 72701

[3]Beckman Institute, California Institute of Technology, Pasadena, CA 91125

*Corresponding Author: nslewis@caltech.edu

Abstract

The size-distribution, coverage, electrochemical impedance, and mass-transport properties of H_2 gas-bubble films were measured for both planar and microwire-array platinized n^+-Si cathodes performing the hydrogen-evolution reaction in 0.50 M H_2SO_4(aq). Inverted, planar n^+-Si/Ti/Pt cathodes produced large, stationary bubbles which contributed to substantial increases in ohmic potential drops. In contrast, regardless of orientation, microwire array n^+-Si/Ti/Pt cathodes exhibited a smaller layer of bubbles on the surface, and the formation of bubbles did not substantially increase the steady-state overpotential for H_2(g) production. Experiments using an electroactive tracer species indicated that even when oriented against gravity, bubbles enhanced mass transport at the electrode surface. Microconvection due to growing and coalescing bubbles dominated effects due to macroconvection of gliding bubbles on Si microwire array cathodes. Electrodes that maintained a large number of small bubbles on the surface simultaneously exhibited low concentrations of dissolved hydrogen and small ohmic potential drops, thus exhibiting the lowest steady-state overpotentials. The results indicate that microstructured electrodes can operate acceptably for unassisted solar-driven water splitting in the absence of external convection and can function regardless of the orientation of the electrode with respect to the gravitational force vector.

Keywords

Solar-energy, hydrogen, electrochemistry, solar-water-splitting, silicon

TOC

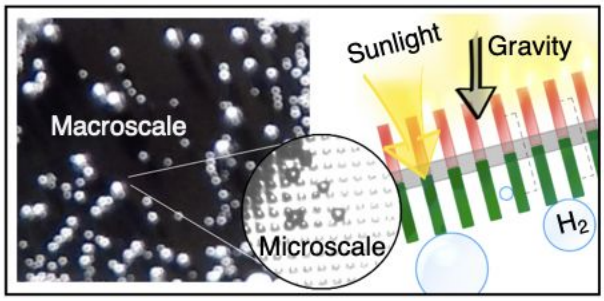

Silicon microwire-arrays mitigate the effects of gas bubbles on the total overpotential of hydrogen evolving cathodes oriented against gravity.

Introduction

Fully integrated solar-driven water-splitting devices produce H_2(g) and O_2(g) from sunlight and water.[1-3] One common feature of such systems is the production of bubbles of H_2(g) or O_2(g) on both the side facing the sunlight and on the dark, downwards-facing side of the device, once the dissolved concentration of H_2(aq) and O_2(aq) sufficiently exceeds the saturation condition to surpass the free-energy barrier to nucleation.[4-6] Bubbles can deleteriously refract light away from the light absorber;[7] can preclude effective contact between the liquid electrolyte and the absorber or electrocatalyst;[8-9] and can affect mass transport of species in the boundary layer as well as in the internal volume of porous, structured electrodes. In small-scale laboratory demonstration systems, effects of bubbles are often minimized by vigorously stirring the solution and/or by testing the electrodes in a side-facing or upwards-facing geometry.[1] In most device configurations that are contemplated for use in the field, active stirring of the electrolyte over large areas is not practical.[3] Management of gas coverage is of minimal concern for research-scale devices, < 1 cm^2 in area, but is regularly considered for industrial-scale electrodes, such as downward-facing, CO_2(g)-evolving anodes required for aluminum manufacturing, in which the thickness of bubble fronts moving across the surface can exceed 1 cm.[10]

Under non-concentrated sunlight, dual-junction tandem photoelectrochemical devices can display solar-to-hydrogen (STH) efficiencies up to 29.7%, corresponding to absolute photocurrent densities for hydrogen evolution, $|J_{H_2}|$, of 24 mA cm^{-2}.[11] Fully integrated designs, including an ion-conducting membrane for product separation, have demonstrated STH conversion at J = 8.5 mA cm^{-2} in 1.0 M KOH(aq) and J = 5.7 mA cm^{-2} in 1.0 M H_2SO_4(aq).[12-13] A dual-junction GaInP/GaInAs photocathode wired to a separated anode exhibited $|J_{H_2}|$ = 15.7 mA cm^{-2} in 1.0 M $HClO_4$(aq).[14] Higher current densities are possible for photoelectrochemical devices under

concentrated sunlight, and a triple-junction InGaP/InGaAs/Ge photoabsorber integrated with a gas-diffusion electrode under a 4 L min^{-1} flow of H_2O as both the reactant and coolant exhibited $|J_{H_2}|$ = 880 mA cm^{-2} based on the area of the electrolyzer components.[15]

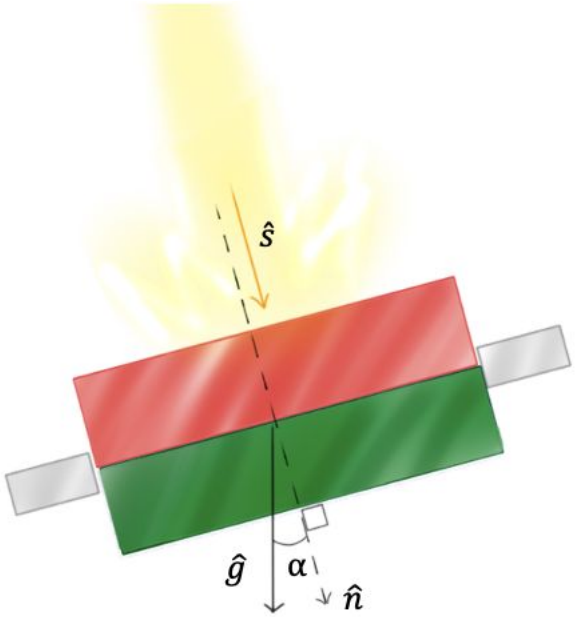

Scheme 1: Monolithic, integrated tandem solar-to-fuel device, with a wide band-gap semiconductor represented in red, a narrow band-gap semiconductor represented in blue, embedded in a gray membrane for product separation. The orientation, α, is defined as the angle between the gravitational vector and the surface normal of the bottom side of the device. Optimal solar collection occurs when $\hat{n} \cdot \hat{s}$ approaches 1. The path of current-carrying charged species is represented as a dotted line.

Studies of the hydrogen-evolution reaction (HER) have provided a detailed understanding of the nucleation and growth behavior of individual H_2(g) bubbles.[4, 16-18] Capillary forces at structured electrode surfaces provide a mechanism for reducing the adhesive force of gas bubbles. Moreover, "aerophobic" electrodes prepared from nanostructured metals and light absorbers effect a reduction in the diameter of departing bubbles due to increased wettability of the surface.[19-21] Photoelectrochemical H_2 evolution from an InP photocathode modified with nanostructured Rh has been investigated in a microgravity environment,[22] and under simulated sunlight yielded $|J_{H_2}|$

> 14 mA cm^{-2} for 9 s in 1.0 M $HClO_4$ containing 1% (v/v) isopropyl alcohol. Si microwire, μW, array electrodes exhibit a low gas coverage during H_2 evolution due to the increased wettability of the surface relative to a planar Si electrode.[23] Tandem device designs evolving separate streams of combustible gases require at least one downward-facing electrode, generating either H_2 or O_2 (Scheme 1), but the effects of electrochemical generation of gases at rates relevant to efficient solar fuels generation, while opposing gravity and without external forced convection, are not well understood. Vertically oriented Si μW arrays, having diameters approximately equal to the minority-carrier diffusion length and having heights large enough to be embedded in ion-conducting membranes, are a technologically-relevant model system for studies of gas evolution in integrated solar fuels generation systems.[24]

We report herein the electrochemical behavior of representative planar and microwire-array cathodes prepared from n^+-Si(100) surfaces metalized with a continuous layer of Pt, to understand how the geometry and orientation of these electrodes control the size-distribution and coverage of H_2(g) bubbles. Moreover, the effects of H_2 evolution on the electrochemical behavior of the dark, downward-facing side of an integrated solar-driven water-splitting device, including effects on mass transport-limited current densities, the concentrations of dissolved H_2 near the electrode surface, and resistance drops at the cathode, have been elucidated through extensive measurements of bubble size distributions and coverages.

Results

Figure 1 presents scanning-electron micrographs of n^+-Si microwire arrays after metallization with Ti/Pt. Deep reactive-ion etching of patterned n^+-Si(100) surfaces produced μW arrays over cm^2 areas with the microwires highly uniform in diameter, pitch, and height. Deposition of Pt by sputtering did not substantially modify the geometry or surface roughness of

the array. Arrays were etched to a height of 30 μm, and three array geometries: (as defined by the photolithographic mask and etching time; 6 μm diameter and 14 μm center-to-center pitch, μW 6|14; 6 μm diameter and 28 μm pitch, μW 6|28; and 3 μm diameter and 11 μm pitch, μW 3|11) were prepared to investigate the electrochemical effects of variation in microwire spacing and diameter. The diameters and pitches of the arrays were measured via scanning electron microscopy of representative cross sections of the array and were consistent with the predicted dimensions (Figure S1).

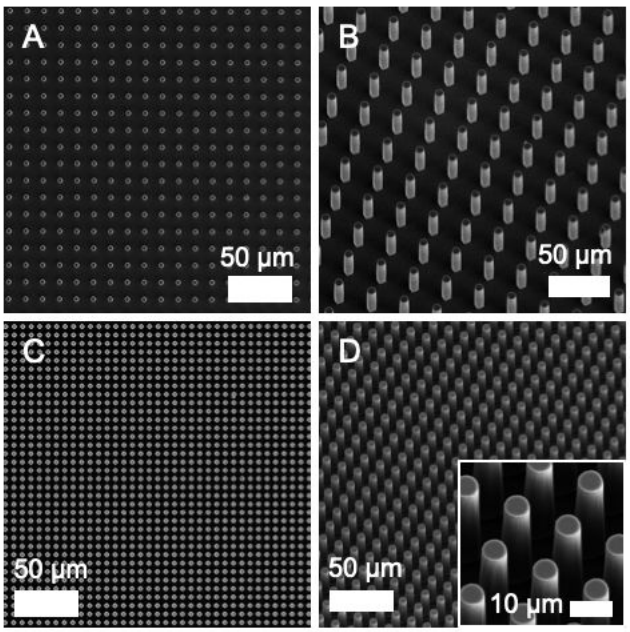

Figure 1: Scanning electron microscope images of platinized n^+-Si(100) microwire arrays of nominal diameter 6 μm, height 30 μm, and pitch 28 μm (A,B) and 14 μm (C,D). Images acquired at normal incidence (A,C), scale bar represents 100 μm; 30 degrees of tilt (B,D) scale bar represents 50 μm, inset scale bar represents 10 μm.

Electrochemical behavior of inverted cathodes

The electrochemical behavior of planar and microstructured n^+-Si/Ti/Pt cathodes were compared in a stagnant cell containing 0.50 M H_2SO_4(aq). Figure 2 displays the time-dependent overpotential, η_T, of planar and microstructured n^+-Si/Ti/Pt cathodes as a function of current density, J, and orientation, α, with α representing the angle between the gravitational vector and

the surface normal of the bottom side of the electrode. At acute angles of α (i.e., predominantly downward-facing electrodes) planar n^+-Si/Ti/Pt electrodes exhibited large η_T relative to the reversible hydrogen potential, RHE, to drive a constant J for the HER, J_{H_2}. The increase in η_T was proportional to the current density, and abrupt decreases in η_T with time correlated with the periodic release of large gas bubbles from the electrode surface (Figure 2B). In contrast, despite the generation of gas bubbles, n^+-Si/Ti/Pt microwire array electrodes exhibited stable, and much lower, values of η_T under chronoamperometric control. Downward-facing ($\alpha \sim 0°$) microwire array and planar electrodes at $|J_{H_2}| < 30$ mA cm^{-2} trapped large gas bubbles and exhibited potentials that were unstable with time, but also showed potentials that were lower on average than the potential exhibited by the same electrode when facing upwards ($\alpha = 180°$) (Figure S2).

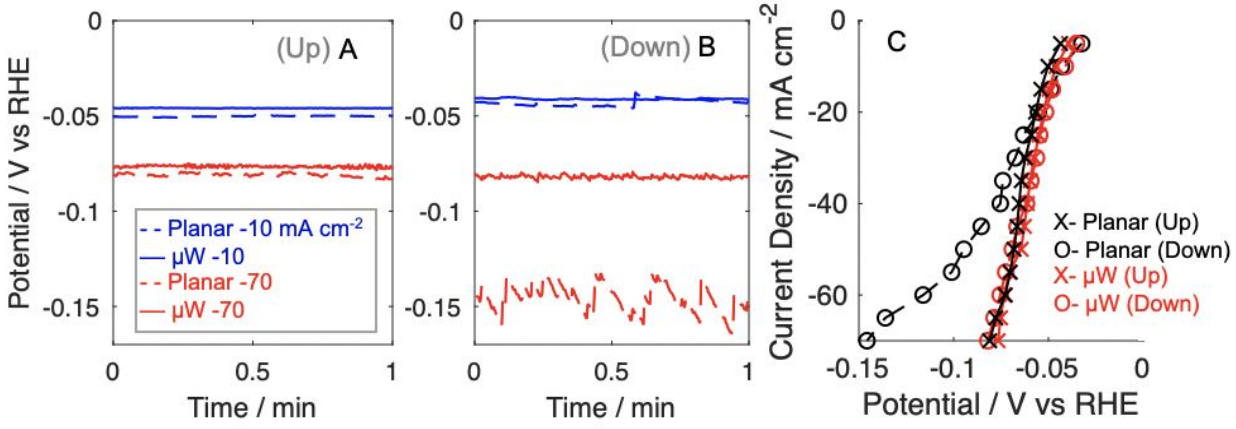

Figure 2: Comparison of the (A) upward-facing and (B) downward-facing electrochemical behavior of galvanostatically controlled planar and microstructured cathodes, respectively, in 0.50 M H_2SO_4(aq) as a function of current density. Planar Pt electrodes are represented by dashed lines and μW 6|14 electrodes are represented by continuous lines. Devices behaved mutually similarly when facing upward but at high current, inverted planar Pt exhibited increased overpotentials relative to microstructured electrodes. (C) Comparison of the average potential required to produce a constant current density at a planar Pt electrode, black, and a μW 6|14 electrode. Upward-facing behavior is represented by x's, downward facing behavior is represented by open circles.

Physical characterization of bubble films

To investigate the role of gas coverage on fluctuations in the overpotential, electrochemical experiments were performed in tandem with macroscopic and microscopic imaging of the electrode surface. Figure 3 shows changes in the fractional gas coverage, Θ, as a function of time for n^+-Si/Ti/Pt electrodes held at J = -30 mA cm^{-2}. Inverted (α = 15°) planar n^+-Si/Ti/Pt electrodes exhibited a time-dependent value of Θ that was positively correlated with the absolute overpotential relative to RHE (Figure 3A), with greater changes in η_T occurring at larger $|J_{H_2}|$ (Figure S3). In contrast, regardless of orientation, microstructured n^+-Si/Ti/Pt electrodes exhibited stable η_T and Θ values over time (Figure 3B-D). At $|J_{H_2}|$ > 100 mA cm^{-2}, potential instabilities at planar electrodes became more frequent and smaller in magnitude, whereas microwire array electrodes exhibited a stable η_T (Figure S4). The average value of Θ at a given $|J_{H_2}|$ was a function of the geometry of the n^+-Si/Ti/Pt microwire array. At $|J_{H_2}|$ = 30 mA cm^{-2}, μW 6|14 electrodes exhibited an average Θ = 15%, whereas μW 3|11 and μW 6|28 electrodes exhibited an average Θ = 41% and 52%, respectively. Additional Θ data for various electrodes as a function of current density are presented in Figure S5. Despite the variation in Θ for electrodes of different microwire array geometries, values for η_T were relatively insensitive to the μW array geometry, indicating that gas coverage alone was not a strong predictor of the chronopotentiometric behavior (Figure 2B-D). Notably, μW 6|28 cathodes maintained low overpotentials for the HER despite having gas coverages comparable to those of planar n^+-Si/Ti/Pt electrodes. For planar, μW 3|11, and μW 6|28 electrodes, Θ increased asymptotically as $|J_{H_2}|$ increased, although the stable value of Θ depended on the microstructure of the electrode. For μW 6|14 electrodes, the gas coverage was suppressed and only increased noticeably when $|J_{H_2}|$ > 60 mA cm^{-2} (Figure S5).

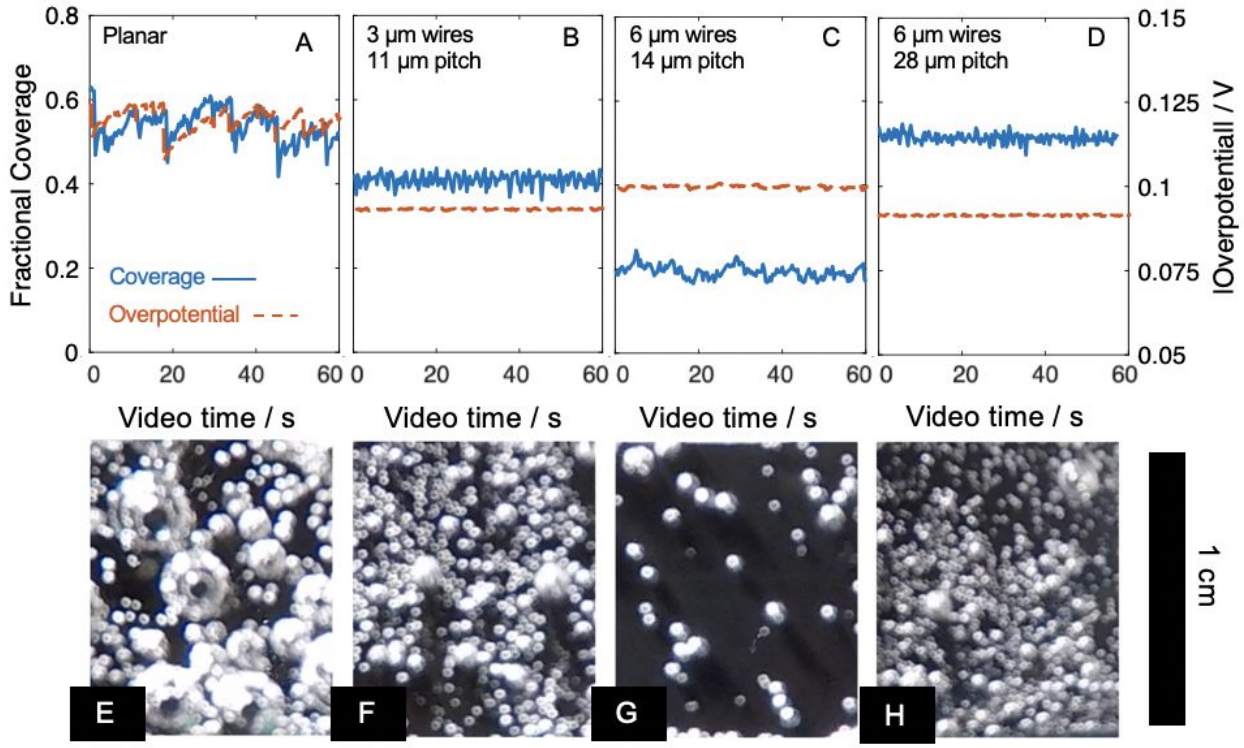

Figure 3: (A-D) Comparison of fractional gas coverage of downward-facing n^+-Si/Ti/Pt cathodes, at α = 15°, at -30 mA cm^{-2} in 0.50 M H_2SO_4(aq), relative to the absolute overpotential for the HER in 0.50 M H_2SO_4(aq) as a function of time. (E-H) Representative images from videos recorded at 60 frames s^{-1} of downward-facing cathodes passing a current density of 30 mA cm^{-2} for the HER. (A,E) planar n^+-Si(100); Si microwire arrays with a width and pitch, respectively of: (B,F) 3 and 11 μm; (C,G) 6 and 14 μm; and (D,H) 6 and 28 μm. Scale bar represents 1 cm.

The primary difference between the gas bubble layer that covered μW and planar n^+-Si/Ti/Pt electrodes was the size of the bubbles (Figure 3E-H). Additional images as a function of $|J_{H_2}|$ are presented as Figure S6-S7 and Movie S1-S2. Figure S8 presents the time-dependent mean bubble diameters, weighted by the relative projected area of the bubbles, $\overline{d}_w$, for various n^+-Si/Ti/Pt electrodes at α = 15° as a function of $|J_{H_2}|$. At α = 15° and $|J_{H_2}|$ = 30 mA cm^{-2}, $\overline{d}_w$ at planar n^+-Si/Ti/Pt electrodes varied between 0.5 and 3 mm, whereas $\overline{d}_w$ was consistently < 0.6 mm at μW 6|14 and μW 3|11 electrodes. The variation in Θ for different microwire array geometries was caused by a difference in the number density of bubbles, *N*, as opposed to a difference in the size

of the bubbles adhering to the surface (Figure S9A). Increasing $|J_{H_2}|$ at inverted, planar n^+-Si/Ti/Pt electrodes led to lower, more stable $\overline{d}_w$ due to a greater *N* on the surface, whereas for $|J_{H_2}| \leq 50$ mA cm^{-2}, inverted μW 6|14 electrodes exhibited a bubble number density that was essentially independent of the applied current density (Figure S9B-C) . The number density and weighted mean diameter were stable for 16 h of testing at -30 mA cm^{-2} (Figure S10). The value of η_T for μW 3|11 n^+-Si/Ti/Pt cathodes at -30 mA cm^{-2} was stable with respect to bubble coverage but η_T increased from 47 mV to 174 mV after 16 h (Figure S11A). At $|J_{H_2}|$ = 100 mA cm^{-2}, planar and μW-array n^+-Si/Ti/Pt cathodes both exhibited a continual increase in η_T (Figure S11B-C).

To investigate the mechanism behind differences in *N* as a function of microstructure, the detachment and growth behavior of gas bubbles were measured via high-speed microscopy on upward-facing electrodes. Figure 4 presents the growth and detachment behavior for bubbles released from an upward-facing μW 6|28 electrode during 20 s of hydrogen evolution at $|J_{H_2}|$ = 50 mA cm^{-2}. In contrast to downward-facing electrodes, upward-facing μW 6|28 electrodes exhibited low *N* and Θ values. Once the bubble diameter exceeded the pitch of the array, within ms individual bubbles that nucleated within the voids of the microwire array were forced away from the surface (Figure S12). On upward-facing electrodes, the mean departure diameter was not a function of the spacing between microwires, with mean departure diameters at a μW 6|14 and μW 6|28 electrode having values of 370 ± 150 μm and 330 ± 170 μm, respectively (Figure S11). Repetitive nucleation was frequently observed at locations on the electrode surface that also exhibited large departure diameters (Figure S13). For bubble growth that is limited by radial transport of H_2(aq) to the surface, the radius, *R*, of a bubble as a function of time, *t*, is given by $R(t) = \tilde{b}(Dt)^{1/2}$, where *D* is the diffusion coefficient of the gas and $\tilde{b}$ is the dimensionless growth coefficient.[16] At $|J_{H_2}|$ = 50 mA cm^{-2}, values of $\tilde{b}$ indicated that bubble growth velocities were controlled by diffusion; were

stable at isolated sites after 10 s (Figure S14); and were variable as a function of position on the electrode (Figure 5D). New nucleation sites continued to form throughout the 20 s measurement, indicating that nucleation was adequately described by classical heterogeneous nucleation theory and the formation of bubbles was thus not limited to preexisting gas cavities.[30]

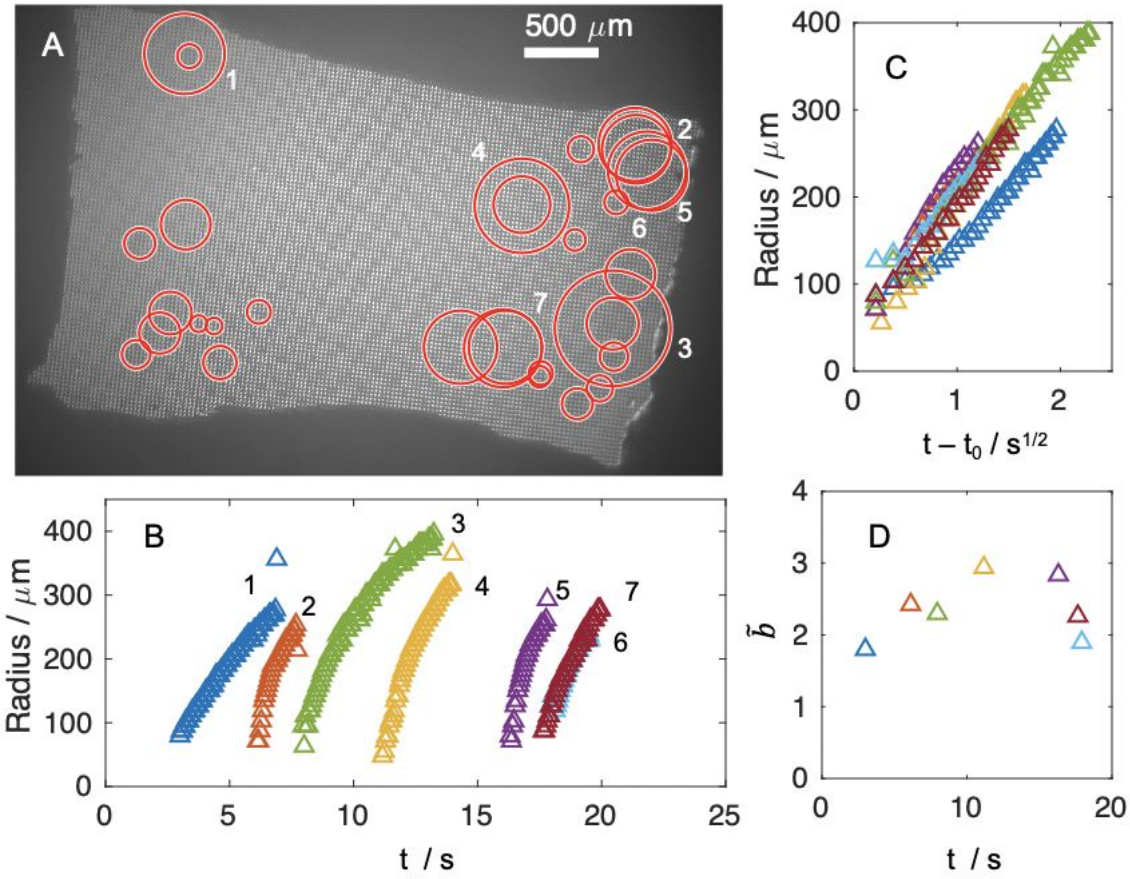

Figure 4: High-speed microscopy measurements of an upward-facing μW 6|28 electrode held at -50 mA cm^{-2} for 20 s in 0.50 M H_2SO_4 (aq). (A) Map of departure diameters measured during a single experiment. (B) Representative radius versus time traces measured via image processing software, with sites labeled in (A). (C) Radius versus square root of bubble growth time, where t_0 is the experiment time at nucleation, and (D) calculated $\tilde{b}$ for data presented in (B).

Mass transport properties of bubble films

The effects of gas evolution on the mass-transport properties of inverted cathodes at α = 15° were investigated by use of a redox-active species, ferric sulfate, as Fe^{3+}(aq), as a probe (Figure 5A, S15). Following a 10 min bulk electrolysis at fixed total current density, the total quantity of

Fe^{3+}(aq) that was reduced to Fe^{2+}(aq) was determined spectroscopically (Figure S16-S17). Measurements in a stagnant cell with a Au microelectrode confirmed that the reduction of Fe^{3+}(aq) was mass-transport limited at potentials relevant to sustained H_2 evolution, and moreover confirmed the presence of Fe^{2+}(aq) following electrolysis (Figure S18). In the absence of both $|J_{H_2}|$ and external convection, $|J_{Fe}|$ decayed to < 0.5 mA cm^{-2} within 45 s (Figure S19). At gas-evolving electrodes, the mean mass-transport-limited current density vs time for Fe^{3+}(aq) reduction, $|J_{Fe}|$, was proportional to $|J_{H_2}|$ but the response depended on the electrode surface (Figure 5B). Larger $|J_{Fe}|$ values were observed for μW n$^+$-Si/Ti/Pt surfaces relative to planar n$^+$-Si/Ti/Pt electrodes, regardless of the gas coverage. μW 6|28 electrodes exhibited the largest $|J_{Fe}|$ values at all current densities.

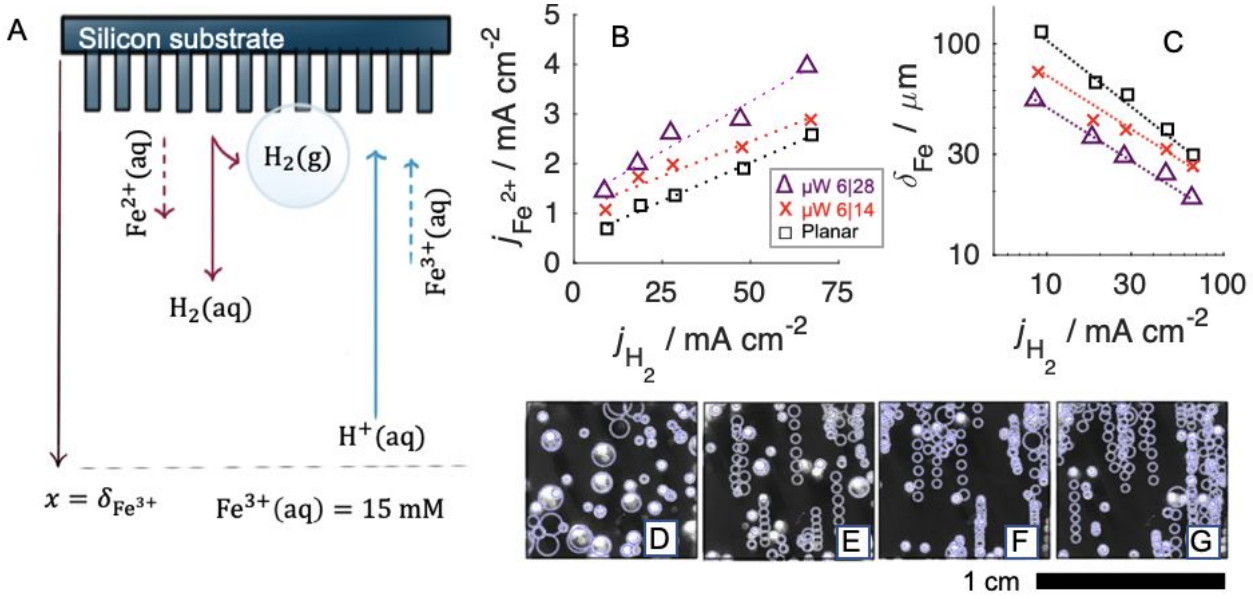

Figure 5: (A) Scheme of experimental procedure for diffusion-limited current experiments (B) Diffusion-limited current density measured via spectrophotometric determination of Fe^{2+}(aq) from 15 mM Fe^{3+}(aq) in 0.50 M H_2SO_4(aq), as a function of current density towards the HER, for various cathodes. Inverted (α = 15°) planar, μW 6|28, and μW 6|14 electrodes are represented as black squares, purple triangles, and red x's respectively, with dotted guidelines. (C) Length of the concentration boundary layer, assuming planar diffusion with the surface concentration of Fe^{2+} approaching zero. (d-g) Representative traces of gas bubbles at an inverted (α = 15°) μW

6|14 electrode passing -10 (D), -30 (E), -50 (F), and -70 mA cm^{-2} (G) sampled over 0.100 s and superimposed over a single image.

To calculate the concentration boundary layer thickness, δ_{Fe}, from J_{Fe}, the diffusion boundary layer was approximated as a continuous, stagnant layer (Equation 1):

$$\frac{J_O}{nF} = \frac{D_O}{\delta_O}\left[C_O^* - C_O|_{x=0}\right] \quad (1)$$

where D_O is the diffusion coefficient of the oxidized species, n = -1, F is Faraday's constant, C_O^* is the bulk concentration of the oxidized species and $C_O|_{x=0}$ is the concentration at the surface. Values for δ_{Fe} at inverted n$^+$-Si/Ti/Pt microwire array electrodes, as calculated from J_{Fe}, were inversely proportional to $|J_{H_2}|$ and were between 30 μm and 100 μm across the range of current densities relevant to a solar fuels device. (Figure 5C). For an inverted (α = 15°) μW 6|14 electrode operated at $|J_{H_2}|$ = 10, 30, 50, 70 mA cm^{-2}, representative traces of gas bubbles were sampled over 0.100 s and superimposed over a single image (Figure 5D-G). The total gas coverage was not sensitive to current density (Figure 2), but increases in current density resulted in a substantially larger fraction of bubbles that were in motion.

Electrochemical impedance of bubble films

The effect of the gas bubble layers on the series resistance, R_{sol}, as a function of time was probed via galvanostatic impedance measurements. The measurements were performed at a frequency for which the impedance was predominantly determined by the solution resistance. Figure S20 presents representative Nyquist plots, comparing the real and imaginary components of the impedance as a function of frequency, for μW 6|14, μW 3|11, and planar electrodes, respectively. Planar electrodes at α = 15° exhibited η and R_{sol} values that were more variable with time than the corresponding values for planar electrodes at α = 90°. For planar electrodes at $|J_{H_2}|$ = 30 mA cm^{-2}, the additional ohmic drop, ΔE_{ohm}, due to the presence of a bubble layer was 22 ± 7

mV at α = 15° and was 6 ± 2 mV at α = 90°. Figure S21 presents chronopotentiometric traces obtained at planar Pt cathodes as a function of α and $|J_{H_2}|$, overlaid with an envelope representing one standard deviation in ΔE_{ohm} calculated from measurements of R_{sol}. The variance in ΔE_{ohm} accounted for the majority of the fluctuations in the electrode potential with time.

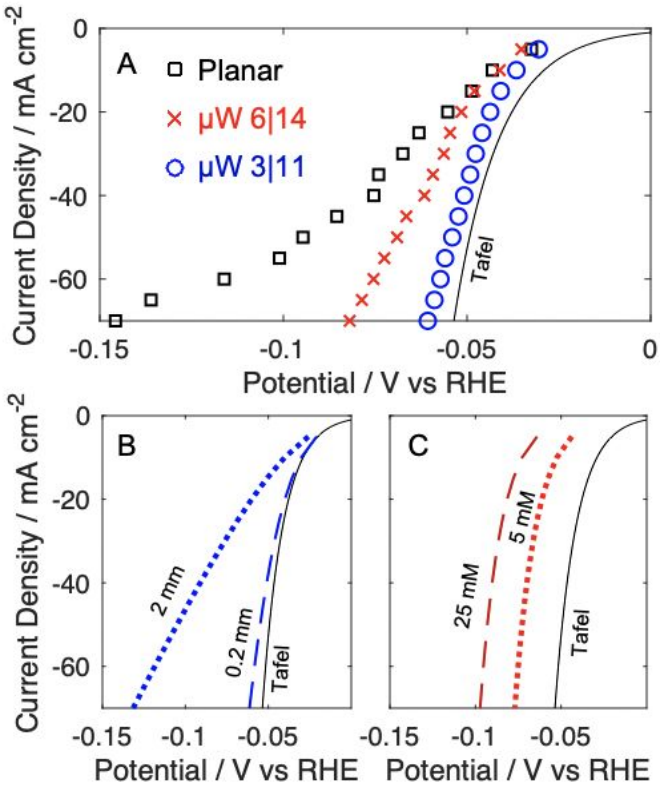

Figure 6: (A) Comparison of the steady-state *J-E* behavior for the HER for planar (black squares), μW 6|14 (red x's), and μW 3|11 electrodes (blue circles), in a downward configuration at α = 15° in 0.50 M H_2SO_4(aq). (B) Comparison of the simulated *J-η* behavior of a Pt cathode covered by a 1 mm (dotted blue line) or a 3 mm thick (dashed blue line) close-packed bubble layer. (C) Comparison of the simulated *J-η* behavior of a Pt cathode in the presence of $C_{H_{2(aq)}}$ = 5 and 25 mM, depicted as dotted and dashed red lines, respectively.

Figure 6A presents the average current density vs. overpotential relationship for planar, μW 6|14, and μW 3|11 n^+-Si/Ti/Pt electrodes, respectively, at α = 15° after correcting for ΔE_{ohm} due to the R_{sol} value measured at 0.0 V versus RHE. For comparison, the ideal current vs.

overpotential behavior predicted for a planar Pt surface with a Tafel slope of 29 mV dec^{-1}, in the absence of mass-transport limitations, is shown as a continuous black line (Equation 2):

$$\eta_{Tafel} = a + b\log_{10}|J| \quad (2)$$

where a and b are the empirical Tafel parameters. Planar n$^+$-Si/Ti/Pt electrodes exhibited substantial deviations from Tafel behavior at all current densities, and the J-η relationship was linear rather than exponential. n$^+$-Si/Ti/Pt μW array electrodes exhibited decreased deviations from Tafel behavior and the J-η relationship was exponential for $|J_{H_2}|$ < 50 mA cm^{-2}.

The relative contributions of ohmic drop, catalyst surface area, and increased concentration of H_2(aq) can be separated into different classes of overpotentials. At an electrode surface covered by gas bubbles at constant current, an additional overpotential required due to an increase in effective current density at sites not covered by gas bubbles is given by Equation 3:

$$\eta_h = b\log_{10}[A/A'] \quad (3)$$

where η_h represents the hyperpolarization, and is dependent on the ratio of A to the remaining active area A'.[9] In the absence of gas bubbles, accumulation of H_2(aq) in the boundary layer shifts the local reversible hydrogen electrode potential as predicted by a Nernstian relationship (Equation 4):

$$\eta_C = 2.3\frac{RT}{nF}\log\left[C_{H_2}|_{x=0}/C^*_{H_2}\right] \quad (4)$$

where R is the gas constant, F is Faraday's constant and n is the number of electrons involved in the reaction.

The measured ohmic drop contribution was compared to the resistance of a hypothetical layer of gas bubbles with a single thickness, L, and void fraction, f_g. The effective conductivity, K_m, of a mixed-phase layer was calculated from Maxwell's equation (Equation 5):

$$K_m = (1 - f_g)/(1 + \frac{f_g}{2}) \quad (5)$$

and used to estimate the additional ohmic drop during gas evolution (Equation 6):

$$\Delta E_{ohm} = \frac{iL(1-K_m)}{\kappa K_m} + \left[\frac{iL}{\kappa}\right] \quad (6)$$

where κ is the solution conductivity,[25] with the ohmic drop present in the absence of gas bubbles contained within brackets, and $\Delta E'_{ohm}$ represents the remaining ohmic drop after removal of this term.[9, 26]

The total potential drop between the cathode and reference electrode, following correction for the cell resistance, can be expressed by Equation 7:[9]

$$\eta_T = \Delta E'_{ohm} + \eta_{Tafel} + \eta_h + \eta_C \quad (7)$$

Equation 7 was used to simulate the *J*-η relationship of H_2-evolving cathodes as a function of varied f_g, L, and $C_{H_{2(aq)}}$. A quantitative comparison between the coverage of gas bubbles and the observed overpotentials was not performed, due to the difficulty of quantifying L at electrode surfaces that were covered by bubbles exhibiting diameters that varied with position and time. The peak weighted mean diameter of bubbles attached to planar and μW 3|11 electrodes at -30 mA cm^{-2} was 2 mm and 0.2 mm, respectively (Figure S8). Simulated *J*-*E* data for a hypothetical close packed layer of gas bubbles with these values of L are presented as Figure 6B. Increasing f_g from 0.3 to 0.6, near the limit for a single layer of hexagonally close-packed spheres, increased the overpotential at $|J_{H_2}|$ = 30 mA cm^{-2}, η_{30}, by 5%, whereas increasing the thickness of the bubble layer to 3 mm increased η_{30} by 44% (Figure 6C). Relative to a bare Pt surface, decreases of 30% and 60% in the catalyst surface area due to bubble coverage led to an increase in η_{30} of 9% and 23%, respectively. Increasing the local $C_{H_{2(aq)}}$ to 5 mM or 25 mM led to an increase in η_{30} of 53% and 102%, respectively, relative to a cathode with a surface $C_{H_{2(aq)}}$ = 0.78 mM.

Discussion

The capillary forces due to electrolyte infilling of μW arrays exceed the buoyant forces due to gravity, and thus prevent obstruction of μW electrode surfaces by bubbles, regardless of α. Microwire array electrodes exhibit smaller adhesive forces towards gas bubbles than planar electrodes, leading to more rapid release of bubbles and more stable η_T. Adhesion of individual gas bubbles could occur exclusively at the top face of microwires, known as the Cassie-Baxter state, or additionally at the sidewalls and substrate, known as the Wenzel state.[27] Mutually similar departure diameters were measured via high-speed microscopy for μW 6|14 and μW 6|28 electrodes, which is inconsistent with an adhesion process that depends on the internal surface area of the microwire array but is consistent with adhesion being dominated by the top-facing area of an individual microwire or defect site. Results from this work extend a prior study that demonstrated stabilized photoelectrochemical behavior of Si μW and nanowire array electrodes at α = 90° due to a reduced Θ relative to planar electrodes,[22-23] and additionally indicate that μW electrodes exhibit chronopotentiometric behavior that is insensitive to Θ even against buoyant force vectors directed antiparallel to the surface normal.

Increases to $C_{H_{2(aq)}}$ and L constituted the largest relative contributions to increased values of η_T at small and large $|J_{H_2}|$, respectively. At $|J_{H_2}|$ = 30 mA cm^{-2} the effects of Θ on f_g and A^* contributed < 10 mV of added overpotential. These results are consistent with the differing chronopotentiometric behavior of μW array and planar electrodes having mutually similar Θ values. These observations suggest that the primary factor leading to stabilized potentials at μW array electrodes is a reduced gas layer thickness due to a decreased departure diameter for H_2 bubbles. Further decreases in bubble layer thicknesses may be obtained by decreasing the tip radius

of the μW array,[24] for example by utilization of Si microcone arrays that have been developed to minimize optical reflection losses at photoelectrodes.[28-29]

Electrodes prepared from μW 6|14 arrays had the highest areal filling fraction of microwires and exhibited the lowest Θ values at all current densities. The differences in Θ for inverted μW 6|14 and μW 6|28 electrode geometries were caused by variations in the density of nucleation sites on the surface, as opposed to differences in the departure diameters of bubbles (Figure S13). Values of Θ measured at μW 6|28 arrays were very sensitive to the orientation of the electrode, whereas μW 6|14 arrays exhibited low values of N and Θ even at $|J_{H_2}|$ > 100 mA cm^{-2} and α = 15° (Figures 3, 4, S3-S5). Due to the high free-energy barrier to forming a new gas-liquid interface, gas bubbles predominately formed at cavities located at defects or at small gas bubbles left behind during release of macroscopic bubbles (Figure S13, S22).[30] The increased filling fraction at μW 6|14 electrodes, relative to μW 6|28 and μW 3|11 electrodes, prevented isolated bubbles from propagating new nucleation sites upon detachment, and resulted in lower values of N and Θ. Studies on isolated Pt nanoelectrodes have shown that $C_{H_{2(aq)}}$ > 0.1 M are required to form new heterogeneous nuclei.[4] The behavior of the μW 6|14 electrodes at macroscale electrode areas in this work demonstrates that only a few such nuclei are needed across the surface to generate sufficient convection to prevent further nucleation. Differences in Θ between inverted μW 6|14 and μW 6|28 electrodes are caused by emergent properties of the microwire arrays that are specific to testing conditions relevant to operation of a solar fuels device, and moreover would not be readily predicted from the characteristics of bubble formation on individual, isolated Si microwires.

In the absence of bubbles, accumulation of H_2(aq) at the surface leads to a substantial η_C, which shifts the *J*-η characteristic towards more negative potentials while maintaining an

exponential relationship between J and η. Such behavior is consistent with the comparison of steady-state overpotentials at downward-facing μW-array electrodes (3B-D, S2) suggesting that a decrease in Θ led to an increase in $C_{H_{2(aq)}}$ at the surface due to the absence of liquid-gas interfaces available to collect H_2(aq). This result is consistent with the observation of increased overpotentials at -10 mA cm^{-2} for upward-facing electrodes (Figure 2A-B), which readily detached bubbles, in comparison to downward-facing electrodes. At low $|J_{H_2}|$ the voltage loss due to $\Delta E'_{ohm}$ is small in comparison to η_C so the presence of bubbles consequently led to a lower $C_{H_2(aq)}$ and lower η_T at downward-facing electrodes. The linear relationship between R and $t^{1/2}$ for bubbles on upward-facing microwire arrays demonstrated that bubble growth was controlled by transport of dissolved H_2 to the gas-liquid interface from a fluid volume comparable to the volume of gas bubbles,[4] which displayed diameters greater by a factor of 10 than the length of individual microwires. In this respect, the growth behavior of bubbles on microwire arrays is physically similar to the growth behavior at a planar surface. Large dimensionless-growth coefficients were observed at upward-facing microwire array electrodes, which have been used to determine $C_{H_{2(aq)}}$ (Figure S14),[31] however $\tilde{b}$ values measured at $|J_{H_2}|$ > 10 mA cm^{-2} were too large to ignore the effects of advection (Supporting Information).[32] Because η_C is inversely proportional to n, concentration overpotentials incurred during the oxygen-evolution reaction (n = 4) will be reduced relative to overpotentials during the HER (n = 2). Assuming that O_2 and H_2 exhibit similar degrees of supersaturation prior to nucleation,[4-5] evolving O_2 on the top side of a solar-fuels device will lead to reduced total concentration overpotentials because low gas coverages on the top side of a device are likely to lead to an increase in supersaturation of the electrochemical reaction product in the electrolyte.

Despite the physical obstruction of electrolyte responsible for mass transport of reactants and products, the generation of gas bubbles led to an increased $|J_O|$ in comparison to $|J_O|$ in a stagnant electrolyte (Figure 5). Assuming that the Faradaic efficiency for H_2(g) evolution is not a strong function of J_{H_2}, over the range of 10-70 mA cm^{-2},[33] transport of Fe^{3+}(aq) to the electrode surface was driven by volumetric displacement of electrolyte due to H_2 evolution (Figure 5B). Platinized Si μW arrays consistently exhibited larger $|J_{Fe}|$ values than planar n^+-Si/Ti/Pt electrodes, regardless of gas bubble coverage, however the largest $|J_{Fe}|$ values were observed at the arrays that had the largest Θ values. The relationship between δ and J_{H_2} is consistent with theoretical relationships for mass transport driven by microconvection or fluid penetration during individual bubble detachment, for which $\delta \sim J_{H_2}{}^{-1/2}$, as opposed to macroconvection driven by rising bubble films, for which $\delta \sim J_{H_2}{}^{-1/3}$.[34] Comparable values for δ have been measured via $Ce^{3+/4+}$ potentiometric titration for Pt foils at α = 90° and 180° evolving O_2(g) or H_2(g) in 1.0 M H_2SO_4(aq).[35] Previous investigations have inferred that surface roughness did not have substantial effects on δ or that the decreased δ was a function of the increased nucleation density.[36-37] The results in this work, for electrodes with explicitly controlled microstructure, at α = 15°, and at current densities relevant to solar-fuels devices, demonstrate that surface adhesion and microconvection are the dominant independent variables controlling the mass transport properties of bubble films, as opposed to nucleation density or buoyancy-driven convection. For electrodes oriented against $\hat{g}$ in a stagnant electrolyte, the generation of bubbles increases reactant influx and product efflux such that mass transport will not limit device performance.

Collectively, the results obtained for inverted cathodes suggest that efficient and stable electrochemical generation of gases can be obtained via control of the electrode microstructure. When oriented against gravity, the low adhesive force and high number density of bubbles at μW

3|11 and μW 6|28 electrodes lead to thin layers of gas bubbles that exhibit a low resistance, yielding electrochemical behavior that is insensitive to Θ. Notably, μW electrodes that maintained a high N and Θ exhibited the largest mass transport coefficients and lowest η. In contrast, at J_{H_2} values relevant to solar-fuel device operation in unconcentrated sunlight, the absence of bubbles is not desirable, and produced deleterious increases in η that were comparable to the kinetic overpotential exhibited by a Pt catalyst. Moreover, planar n^+-Si/Ti/Pt electrodes exhibited the worst performance of all of the electrodes studied herein, because they produced large, stationary bubbles that generated the least convection and consequently contributed to a large ΔE_{ohm}. Optimal electrode morphologies and geometries will therefore nucleate bubbles across the surface, keeping $C_{H_{2(aq)}}$ in near-equilibrium with H_2(g) at the operating pressure, and will moreover be structured to quickly detach bubbles from the surface, thereby minimizing the thickness of the gas layer and maximizing local convection. Microcavities and surface functionalization can facilitate nucleation to maintain low $C_{H_{2(aq)}}$ values at the surface.[38-39] Further studies should assess whether electrodes that include membranes containing hydrophobic polymer chains also result in sufficient capillary forces to prevent infilling of gas bubbles, and/or whether further surface modification of the microstructure can prevent such infilling. Although the gas coverage of Pt catalysts was not a substantial contributor to the total η, additional studies should investigate the electrochemical behavior of microstructured electrodes covered by catalysts with increased Tafel slopes, relative to Pt catalyzing the HER, to determine how gas coverage affects less active but earth-abundant catalysts for the HER and OER. The electrodes in this work were degenerately doped and therefore insensitive to the optical effects of gas coverage. Experiments on upward-facing, photoactive microwire electrodes are needed to determine whether high coverages of small gas bubbles are suitable for efficient collection of sunlight.

Experimental Methods

A complete list of materials and an extended experimental methods section is provided in the Supplementary Information.

Fabrication of electrodes: Microstructured Si substrates were prepared via photolithographic patterning of polished Czochralski-grown, <100>-oriented, degenerately doped n-type Si wafers with a resistivity < 0.005 ohm-cm (Addison Engineering, Inc.). Microwires were formed via deep reactive-ion etching of Si at -120-130 °C in an SF_6/O_2 plasma. The geometry of the mask defined the wire width; the ratio of O_2 to SF_6 was tuned to achieve vertical sidewalls; and the wire height was defined by the duration of etching. Metallization was performed in an Orion Series Sputtering system (AJA) at a base pressure of 10^{-7} torr. Ti and Pt films were sputtered sequentially in a 5 mtorr Ar plasma at a deposition rate of ~1 nm min^{-1} and ~2.6 nm min^{-1}, respectively. An ohmic back contact was made to the rear side of the Si with an In-Ga eutectic (Alfa Aesar), and the electrode was affixed to a Cu-Sn wire via conductive Ag epoxy (Ted Pella). The electrode was sealed into a piece of 6 mm diameter borosilicate glass tubing using a chemically resistant epoxy (Hysol 9460) that was cured for >12 h at room temperature. The electrode area was measured using a commercial optical scanner.

Electrochemical measurements: HER characteristics were evaluated in a 4-port electrochemical cell that contained an optical flat at the base of the cell to facilitate viewing of the electrode (Figure S23). Degenerately doped n^+-Si electrodes were used to eliminate the effects of a photoactive substrate and to evaluate the performance under conditions experienced by a downward-facing, dark electrode, where gas coverage does not affect light absorption. The electrolyte was 0.50 M H_2SO_4(aq) (TraceMetal Grade, Fisher) that was purged with H_2(g) for at least 30 min prior to testing, and was purged between experiments to maintain H_2(aq) in

equilibrium with H_2(g) at 1 atm. A saturated calomel electrode served as the reference electrode and a Pt mesh electrode behind a Nafion (Dupont) membrane served as the counter electrode. A constant current or potential was obtained using a Biologic SP-200 potentiostat. The cell was mounted on a leveled surface and the electrode orientation was varied by tilting the electrochemical cell to match the angle defined by custom shims.

Macroscopic video collection and analysis: The gas coverage and the size distribution of bubbles were analyzed from video acquired at 60 frames s^{-1}, at a pixel width of 300 cm^{-1}, using a commercially available high-definition camera mounted on optical posts (Thorlabs). Videos were recorded under illumination provided by a filtered Hg (Xe) lamp. Images were processed in MATLAB. Image thresholding was used to estimate the fractional gas coverage, θ, with black pixels representing the electrode and white pixels representing regions covered by gas bubbles. Bubble size distributions were measured as circles detected within individual images processed via a Hough transform of the grayscale image. Statistics were acquired after at least 2 min of continuous H_2 evolution to allow the behavior of the electrode to stabilize. Large bubbles could not be automatically detected and were therefore measured manually. Bubbles with diameters < 300 μm (~10 pixels) were omitted from macroscale measurements.

Microscopic video collection and analysis: High-speed microscopy experiments were performed in 0.50 M H_2SO_4 (aq) in an HDPE electrochemical cell with a glass cover. The imaging system consisted of a microscope (Olympus BX-53) with a 5x objective, an LED reflectance illuminator (Prior Scientific), and a high-speed camera (Fastec Imaging). All imaging experiments were performed at 200 frames per second. Bubble radii were measured through extended image sequences using routines developed from the SciPy and Scikit-Learn libraries for the Python programming language.

Acknowledgements

This material is based upon work performed by the Joint Center for Artificial Photosynthesis, a DOE Energy Innovation Hub, supported through the Office of Science of the U.S. Department of Energy under Award No. DE-SC0004993. High-speed microscopy experiments were supported by the National Science Foundation under Grant No. 1732096 (R.H.C.). Fabrication of the Si microwire arrays was performed in the Kavli Nanoscience Institute (KNI) at Caltech, and we thank the KNI staff for their assistance during fabrication. We thank K.M.P. and B.S.B. for helpful discussions on experimental design.

Author Contributions

Conceptualization, P.A.K., and N.S.L; Methodology, P.A.K., Investigation, P.A.K. and R.H.C.; Writing — Original Draft, P.A.K. and N.S.L.; Writing — Review & Editing, N.S.L., P.A.K., R.H.C.; Funding Acquisition, N.S.L. and R.H.C.; Supervision, N.S.L.

Declaration of Interests

The authors declare no competing interests.

References

1. J. W. Ager, M. R. Shaner, K. A. Walczak, I. D. Sharp, and S. Ardo, *Energy Environ. Sci.,* 2015, **8**, 2811-2824.

2. J. R. McKone, N. S. Lewis, and H. B. Gray, *Chem. Mater.,* 2013**, 26**, 407-414.

3. S. Ardo, D. Fernandez Rivas, M. A. Modestino, V. Schulze Greiving, F. F. Abdi, E. Alarcon Llado, V. Artero, K. Ayers, C. Battaglia, J. P. Becker, et al., *Energy Environ. Sci.,* 2018**, 11**, 2768-2783.

4. S. R. German, M. A. Edwards, H. Ren, and H. S. White, *J. Amer. Chem. Soc.,* 2018, **140**, 4047-4053.

5. H. Ren, S. R. German, M. A. Edwards, Q. Chen, and H. S. White, *J. Phys. Chem. Lett.,* 2017, **8**, 2450-2454.

6. Q. Chen, L. Luo, H. Faraji, S. W. Feldberg, and H. S. White, *J. Phys. Chem. Lett.,* 2014, **5**, 3539-44.

7. A. E. Dorfi, A. C. West, and D. V. Esposito, *J. Phys. Chem. C,* 2017, **121**, 26587-26597.

8. R. H. Coridan, Z. G. Schichtl, T. Sun, and K. Fezzaa, *ACS Appl. Mater. Interfaces,* 2016, **8**, 24612-24620.

9. J. A. Leistra and P. J. Sides, *J. Electrochem. Soc.,* 1987, **134,** 2442-2446.

10. S. Fortin, M. Gerhardt, and A. Gesing, *Light Metals*, 1984*,* **1984**, 721-741.

11. S. Hu, C. Xiang, S. Haussener, A. D. Berger, and N. S. Lewis, *Energy Environ. Sci.,* 2013**, 6** , 2984-2993.

12. E. Verlage, S. Hu, R. Liu, R. J. Jones, K. Sun, C. Xiang, N. S. Lewis, and H. A. Atwater, H. A., *Energy Environ. Sci.,* 2015, **8**, 3166-3172.

13. W. J. C. Vijselaar, P. Perez-Rodriguez, P. J. Westerik, R. M. Tiggelaar, A. H. M. Smets, H. Gardeniers, and J. Huskens, *Adv. Energy Mater.,* 2019, **9**, 1803548.

14. W.-H. Cheng, M. H. Richter, M. M. May, J. Ohlmann, D. Lackner, F. Dimroth, T. Hannappel, H. A. Atwater, and H.-J. Lewerenz, *ACS Energy Lett.,* 2018, **3**, 1795-1800.

15. S. Tembhurne, F. Nandjou, and S. Haussener, *Nat. Energy,* 2019, **4**, 399.

16. P. van der Linde, P. Peñas-López, A. M. Soto, Á. D. van der Meer, D. Lohse, H. Gardeniers, and D. F. Rivas, *Energy Environ. Sci.,* 2018, **11**, 3452-3462.

17. X. Zhao, H. Ren, and L. Luo, *Langmuir*, 2019, **35***,* 5392-5408.

18. A. Angulo, P. van der Linde, H. Gardeniers, M. A. Modestino, and D. Fernández Rivas, *Joule,* 2020, **4**, 555-579.

19. Y. Shi, and B. Zhang, *Chem. Soc. Rev.,* 2016, **45**, 1529-1541.

20. Y. Li, H. Zhang, T. Xu, Z. Lu, X. Wu, P. Wan, X. Sun, and L. Jiang, *Adv. Func. Mater.*, 2015, **25**, 1737-1744.

21. M. H. Lee, K. Takei, J. Zhang, R. Kapadia, M. Zheng, Y. Z. Chen, J. Nah, T. S. Matthews, Y. L. Chueh, J. W. Ager, et al., *Angew. Chem. Intl. Ed.*, 2012**, 51**, 10760-4.

22. K. Brinkert, M. H. Richter, O. Akay, J. Liedtke, M. Giersig, K. T. Fountaine, and H.-J. Lewerenz, *Nat. Commun.,* 2018**, 9**, 2527.

23. D. V. Esposito, Y. Lee, H. Yoon, P. M. Haney, N. Y. Labrador, T. P. Moffat, A. A. Talin, and V. A. Szalai, *Sus. Energy Fuels,* 2017**, 1**, 154-173.

24. N. S. Lewis, *Nat. Nanotechnol.,* 2016**, 11**, 1010.

25. J. Casas, F. Alvarez, and L. Cifuentes, *Chem. Eng. Sci.,* 2000**, 55**, 6223-6234.

26. P. J. Sides and C. W. Tobias, *J. Electrochem. Soc.,* 1982, **129**, 2715-2720.

27. D. Murakami, H. Jinnai, and A. Takahara, *Langmuir,* 2014, **30**, 2061-2067.

28. S. Yalamanchili, H. S. Emmer, K. T. Fountaine, C. T. Chen, N. S. Lewis, and H. A. Atwater, *ACS Photonics,* 2016**, 3**, 1854-1861.

29. S. Yalamanchili, P. A. Kempler, K. M. Papadantonakis, H. A. Atwater, and N. S. Lewis, *Sus. Energy Fuels,* 2019, **3**, 2227-2236.

30. S. Jones, G. Evans, and K. Galvin, *Adv. Colloid Interface Sci.,* 1999, **80**, 27-50.

31. P. Van Der Linde, A. Moreno Soto, P. Peñas-López, J. Rodríguez-Rodríguez, D. Lohse, H. Gardeniers, D. Van Der Meer, and D. Fernández Rivas, *Langmuir,* 2017**, 33**, 12873-12886.

32. P. S. Epstein, and M.S. Plesset, *J. Chem. Phys.,* 1950**, 18**, 1505-1509.

33. H. Vogt, *Electrochim. Acta,* 1984**, 29**, 167-173.

34. H. Vogt, *Comprehensive Treatise of Electrochemistry*, Springer: 1983, 445-489.

35. L. J. Janssen and J. Hoogland, *Electrochim. Acta,* 1970**, 15**, 1013-1023.

36. L. J. Janssen and J. Hoogland, *Electrochim. Acta,* 1973, **18**, 543-550.

37. M. Fouad, G. Sedahmed, H. El Abd, *Electrochim. Acta,* 1973**, 18**, 279-281.

38. P. Peñas, P. van der Linde, W. Vijselaar, D. van der Meer, D. Lohse, J. Huskens, H. Gardeniers, M. A. Modestino, and D. Fernández Rivas, *J. Electrochem. Soc.,* 2019**, 166**, H769-H776.

39. X. Zhao, R. Ranaweera, and L. Luo, *Chem. Commun.,* 2019, **55**, 1378-1381.